Speeding up quantum dissipative dynamics of open systems with kernel methods

Arif Ullah* and Pavlo O. Dral*

State Key Laboratory of Physical Chemistry of Solid Surfaces, Fujian Provincial Key Laboratory of Theoretical and Computational Chemistry, Department of Chemistry, and College of Chemistry and Chemical Engineering, Xiamen University, Xiamen 361005, China

E-mail: ua2024@xmu.edu.cn; dral@xmu.edu.cn

Abstract

The future forecasting ability of machine learning (ML) makes ML a promising tool for predicting long-time quantum dissipative dynamics of open systems. In this Article, we employ nonparametric machine learning algorithm (kernel ridge regression as a representative of the kernel methods) to study the quantum dissipative dynamics of the widely-used spin-boson model. Our ML model takes short-time dynamics as an input and is used for fast propagation of the long-time dynamics, greatly reducing the computational effort in comparison with the traditional approaches. Presented results show that the ML model performs well in both symmetric and asymmetric spin-boson models. Our approach is not limited to spin-boson model and can be extended to complex systems.

Introduction

With the realization that isolated systems do not exist in the real world, we have to deal with open quantum systems, where we need to consider that the system and the surrounding environment can exchange energy, particles and/or quantum phase. Spin-boson (SB) model is one of the well-known models which is widely used to understand the effects of the surrounding environment on the system. SB model describes a two-state system coupled to infinite number of non-interacting harmonic oscillators. Understanding quantum dissipative dynamics of SB model (or in general open quantum system) has applications in wide range of settings such as quantum computing,[1] quantum memories,[2] quantum electrodynamics,[3,4] organic solar cells,[5] superconducting junctions,[6] quantum biology,[7] quantum optics,[8] quantum transport,[9,10] defect tunneling in solids,[11,12] quantum dots,[13,14] and colour centres and Cooper pair boxes.[15,16] In addition, SB model has remained a key-model for testing and comparison of open quantum system theories before extending them to complex systems. A large number of numerical methods has been developed to study SB model such as numerical renormalization group (NRG) method,[17,18] the density matrix renormalization group (DMRG) method,[19,20] the quantum Monte Carlo (QMC) method,[21,22] the time evolving density matrix using orthogonal polynomial algorithm (TEDOPA),[23,24] the reaction coordinate mapping,[25] the multi-configuration time-dependent Hartree (MCTDH) method[26,27] and its extensions[28] (the Nakajima–Zwanzig generalized quantum master equation (GQME),[29,30] transfer tensor method (TTM)[31–33] and numerical variational method (NVM)[34]). Regardless of their success, these methods have there own limitations in applicability and accuracy.

In addition to these methods, another popular approach is classical mapping-based approach (Meyer–Miller–Stock–Thoss mapping,[35–39] spin-based mapping[40,41] and so on), where system and surrounding environment dynamics is described by classical trajectories. Classical mapping-based approaches are more feasible but because of the classical description, they fail to properly describe the dynamics of the system especially at low temperature. Coming back to exact quantum methods, Makri and coauthors proposed quasiadiabatic propagator

path integral (QUAPI) scheme.[42,43] In QUAPI approach, all correlation effects are included over a finite time $\tau = K\delta t$ and correlation effects beyond τ are neglected. Good convergence requires time τ to be as large as possible and the Trotter increment δt as small as possible. In QUAPI approach, the growing computational cost with the increase of system size and time τ limits its applicability for large complex systems.

An alternative numerical exact bench-marking approach is the hierarchical equations of motion (HEOM)[44–53] approach pioneered by Tanimura and Kubo.[54] HEOM approach captures the combined effects of system–environment dissipation, non-Markovian memory effect, and many-body correlation in a non-perturbative manner. In this approach, a hierarchy of deterministic differential equations are constructed by using a set of memory basis functions to unravel the correlation function of the environment. The size of HEOM depends on two factors; the number of memory basis functions M and the depth of the hierarchy L, which depends critically on the strength of the system–environment interaction and many-body correlation. In the case of low temperature and strong dissipative interaction, good convergence requires large M and L, which inevitably makes HEOM approach rather expensive. Such a drawback has restrained the use of HEOM method in the ultra-low temperature regime.

Another approach with no temperature limitation, is the trajectory-based stochastic equation of motion (SEOM) approach. In stochastic formulation, the influence of environment on the system is captured by stochastic auxiliary fields. The SEOM for boson environment has been established and adopted by many authors.[55–68] Recently, the stochastic approach has been extended to open quantum system with fermion environment.[69–71] Large amount of research work can be found on the applications of SEOM.[72–75] SEOM approach can be used in both low- and high-temperature cases, although at low temperature, a good convergence needs more trajectories. The bottleneck of SEOM approach for complex systems is the increase in the number of noises with the number of states, which as a result makes SEOM approach hard to converge in the long-time limit.

In the past decade, machine learning (ML) has found its applications in all fields of science. In the field of chemical physics, ML has seen many applications,[76,77] such as to construct the potential energy surfaces,[78,79] to learn coarse-grained force fields,[80] atomic partial charges,[81] dielectric constants in crystals,[82] absorption cross sections,[83] and excited state dynamics.[84–86] ML approaches (recurrent neural network and non-linear autoregressive neural networks) have been employed to simulate the quantum dissipative dynamics of SB and Landau–Zener models.[87,88] Recently Rodríguez and Kananenka[89] have used the parametric ML model based on convolutional neural networks to study the excitation energy transfer in a dimer, where they suggested to use short-time dynamics as input for ML. In their approach, ML was trained on reduced density matrix elements and required computationally expensive fitting of ca. 3 million parameters on ca. 4 thousand trajectories. In a recent preprint, Lin et al. used bootstrap-based long short-term memory recurrent neural network to predict the quantum dissipative dynamics.[90]

Realizing the power of nonparametric machine learning algorithms, in this paper, we are utilizing the kernel ridge regression (KRR) model to simulate the quantum dissipative dynamics of very general SB model, which is a typical model for benchmarking different approaches. Nonparametric models based on kernel methods, to which KRR belongs, often provide more accurate ML models as was shown in several independent studies.[91–94] In addition, the problem of fitting KRR parameters has closed solution as it is the convex optimization problem, making KRR attractive for training ML models. In our approach we train the ML model directly on the expectation value of $\hat{\sigma}_z$ (aka the population difference), which is the property of interest, instead of training on the intermediate properties (reduced density matrix elements) as was done previously,[89] thus reducing computational overhead. After training, our KRR model takes rather short-time quantum dynamics as input and predicts the long-time dynamics as an output making our model a promising cost-effective tool for open quantum systems. Interestingly, our approach only required 450 training trajectories and fitting of 72 thousand parameters. It accurately predicts the long-time dynamics

in all cases: from weak to strong system-environment couplings and from weak to strong environment cases. In our study, we included both the symmetric and asymmetric cases of the SB model.

The rest of the paper is organized as follows. In the Theory section, we review the theory of the SB model and present our KRR approach. In Data and Training section, all the steps adopted during training and data preparation are explained. Next section is Results and Discussion which is followed by Concluding Remarks.

Theory

Spin-boson model

The theory behind the SB model is well-explored by many authors,[21,35,44,45,55,56] but for the sake of completeness, we summarize it here too. The well-known SB model describes a two-level system coupled with the outside environment. The environment consists of infinite number of non-interacting harmonic oscillators. The total Hamiltonian is written as ($\hbar = 1$)

$$\begin{aligned} \hat{H} &= \hat{H}_{\mathrm{s}} + \hat{H}_{\mathrm{env}} + \hat{H}_{\mathrm{s-env}}, \\ \hat{H} &= \frac{1}{2}\epsilon\hat{\sigma}_z + \frac{1}{2}\Delta\hat{\sigma}_x + \sum_k \omega_k \hat{b}_k^\dagger \hat{b}_k + \frac{1}{2}\hat{\sigma}_z\hat{F}, \end{aligned} \tag{1}$$

where $\hat{H}_{\mathrm{s}}$, $\hat{H}_{\mathrm{env}}$ and $\hat{H}_{\mathrm{s-env}}$ represent Hamiltonians of the 2-level system, environment and their interaction, respectively. $\hat{\sigma}_x$ and $\hat{\sigma}_z$ are Pauli matrices and ϵ is the energy bias of the two states, i.e., $|e\rangle$ and $|g\rangle$. Δ is the tunneling matrix element of the two states. $b_k^\dagger$ is the creation operator of the environment mode k. The environment mode k interacts with the system via operator $\hat{F}_k = \frac{c_k}{\sqrt{2\omega_k}}(\hat{b}_k + \hat{b}_k^\dagger)$, where c_k is the coupling strength. The total interaction operator F can be written as $\hat{F} = \sum_k \frac{c_k}{\sqrt{2\omega_k}}(\hat{b}_k + \hat{b}_k^\dagger)$.

It is common to consider that at initial time $t = 0$, the interaction between system and the surrounding environment is zero and the environment is in thermal equilibrium state.

The influence of the environment can be described by a two-time correlation function of operator $\hat{F}$, i.e., $C(t) = \langle \hat{F}(t)\hat{F}(0)\rangle$. In the case of no interaction with the system, $C(t)$ can be written as[63]

$$C(t) = \frac{1}{\pi}\int_0^\infty \mathrm{d}\omega J(\omega)\left(\coth\left(\frac{\omega\beta}{2}\right)\cos(\omega t) - \mathrm{i}\sin(\omega t)\right), \tag{2}$$

where $J(\omega)$ is the spectral density

$$J(\omega) = \frac{\pi}{2}\sum_k \frac{c_k^2}{\omega_k}\delta(\omega - \omega_k). \tag{3}$$

As we are only interested in the dynamics of the system, we can trace out the environment degrees of freedom,

$$\hat{\rho}_\mathrm{s}(t) = \mathbf{Tr}_\mathrm{env}\left[\hat{U}(t,0)\hat{\rho}_\mathrm{T}(0)\hat{U}^\dagger(t,0)\right], \tag{4}$$

here $\hat{\rho}_\mathrm{s}(t)$ is the reduced density matrix of the system at time t while $\hat{\rho}(0)$ is the initial density matrix of the composite system governed by $\hat{H}$. $\hat{U}(t,0)$ and $\hat{U}^\dagger(t,0)$ are operators for forward and backward propagation in time, respectively. Different approaches deal with Eq.(4) differently as mentioned in Introduction section. For more details on a specific approach, readers are referred to the corresponding references.

Kernel ridge regression

In kernel ridge regression (KRR), which is also known as Kernel Regularized Least Squares,[95] the approximating function $f(\mathbf{x})$ for a vector of input values $\mathbf{x}$ is defined as[76,96–98]

$$f(\mathbf{x}) = \sum_{i=1}^{N}\alpha_i k(\mathbf{x}, \mathbf{x}_i), \tag{5}$$

here N is the number of training points and $\boldsymbol{\alpha} = \{\alpha_i\}$ is a vector of regression coefficients. The kernel function $k(\mathbf{x}, \mathbf{x}_i)$ takes two vectors $\mathbf{x}$ and $\mathbf{x}_i$ from the input space and measures

the distance between them.

In this work we use the Gaussian kernel as implemented in the MLatom package:[98–100]

$$k\left(\mathbf{x},\mathbf{x}_i\right)=\exp\left(-\frac{\left\|\mathbf{x}-\mathbf{x}_i\right\|_2^2}{2\sigma^2}\right), \tag{6}$$

as our tests showed, it has a good performance for our application and other kernels such as those from a family of popular Matérn kernels are not better. In the Gaussian kernel, we have only one hyperparameter σ, defining the length scale. Intuitively, the Gaussian kernel measures similarity between the vectors $\mathbf{x}$ and $\mathbf{x}_i$. The output of these kernels increases as $\|\mathbf{x}-\mathbf{x}_i\|\to 0$ and becomes unity at $\mathbf{x}=\mathbf{x}_i$, while for large distance $\|\mathbf{x}-\mathbf{x}_i\|\to\infty$, the kernel $k\left(\mathbf{x},\mathbf{x}_i\right)$ tends to zero. After choosing the kernel function, we need to find the regression coefficients $\boldsymbol{\alpha}$ in Eq.(5). It is done by minimization of a squared error loss function[76,97,98]

$$\min_{\alpha}\sum_{i}^{N}\left(f(\mathbf{x}_i)-y_i\right)\right)^2+\lambda\boldsymbol{\alpha}^T\mathbf{K}\boldsymbol{\alpha}, \tag{7}$$

here $\mathbf{y}=\{y_i\}$ is the target output vector, $\mathbf{K}$ is the kernel matrix and λ denotes a non-negative regularization hyperparameter. In above equation, the second term is usually added to stop KRR model from giving too much weight to a single point.[101] After simple algebra, Eq.(7) leads to[96,97]

$$\boldsymbol{\alpha}=\left(\mathbf{K}+\lambda\mathbf{I}\right)^{-1}\mathbf{y}, \tag{8}$$

here $\mathbf{I}$ is the identity matrix.

Data and Training

We consider that our system is initially in the excited state (i.e., $|e\rangle$). For the environment, the Drude–Lorentz spectral density is considered

$$J(\omega) = 2\lambda \frac{\omega\omega_{\mathrm{c}}}{\omega^2 + \omega_{\mathrm{c}}^2}, \tag{9}$$

where ω_c and λ denote the characteristic frequency and the system–environment coupling strength, respectively. In this work, all considered parameters are in atomic units (a.u.). The time-step for integration is $\Delta t = 0.05$ and the time of propagation t_M is fixed to be 20. We generate trajectories of reduced density matrices for all combinations of the following parameters: $\Delta = 1$, $\epsilon \in \{0, 1\}$, $\lambda \in \{0.1, 0.2, 0.3, 0.4, 0.5, 0.6, 0.7, 0.8, 0.9, 1.0\}$, $\omega_c \in \{1, 2, 3, 4, 5, 6, 7, 8, 9, 10\}$, and $\beta \in \{0.1, 0.25, 0.5, 0.75, 1\}$, here $\beta = 1/k_{\mathrm{B}}T$ with k_{B} as Boltzmann constant and T as temperature. It should be noted that we include data for both symmetric and asymmetric SB models, i.e., $\epsilon \in \{0, 1\}$. With the given set of parameters, 1000 trajectories (500 for symmetric and 500 for asymmetric case) of reduced density matrix are generated with the HEOM approach as implemented in the publicly available QuTiP package.[102] As the HEOM method is computationally very expensive at low temperature, we did not include data for very low temperatures. We train our model directly on the data extracted for the expectation value of $\hat{\sigma}_z$ as it is the quantity of interest in the case of spin-boson model. Coming back to training our KRR model, the initial training data are raw trajectories, which can be viewed as unsupervised data. To transform our unsupervised data into supervised training data set, we cut a trajectory at time t_m (memory time using terminology of Rodríguez and Kananenka[89]) and take $\langle\hat{\sigma}_z\rangle$ at the next time step $t_{m+1} = t_m + \Delta t_{train}$ as the target output value (label) y_1 (Fig. 1). The input vector $\mathbf{x}_1$ for KRR consists of $\langle\hat{\sigma}_z\rangle$ values taken from the trajectory with the training time step Δt_{train} within the memory time t_m. The set of input vector and a target value $\{\mathbf{x}_1, y_1\}$ forms the first training point. For the next training point, we shift the time-window by one time step

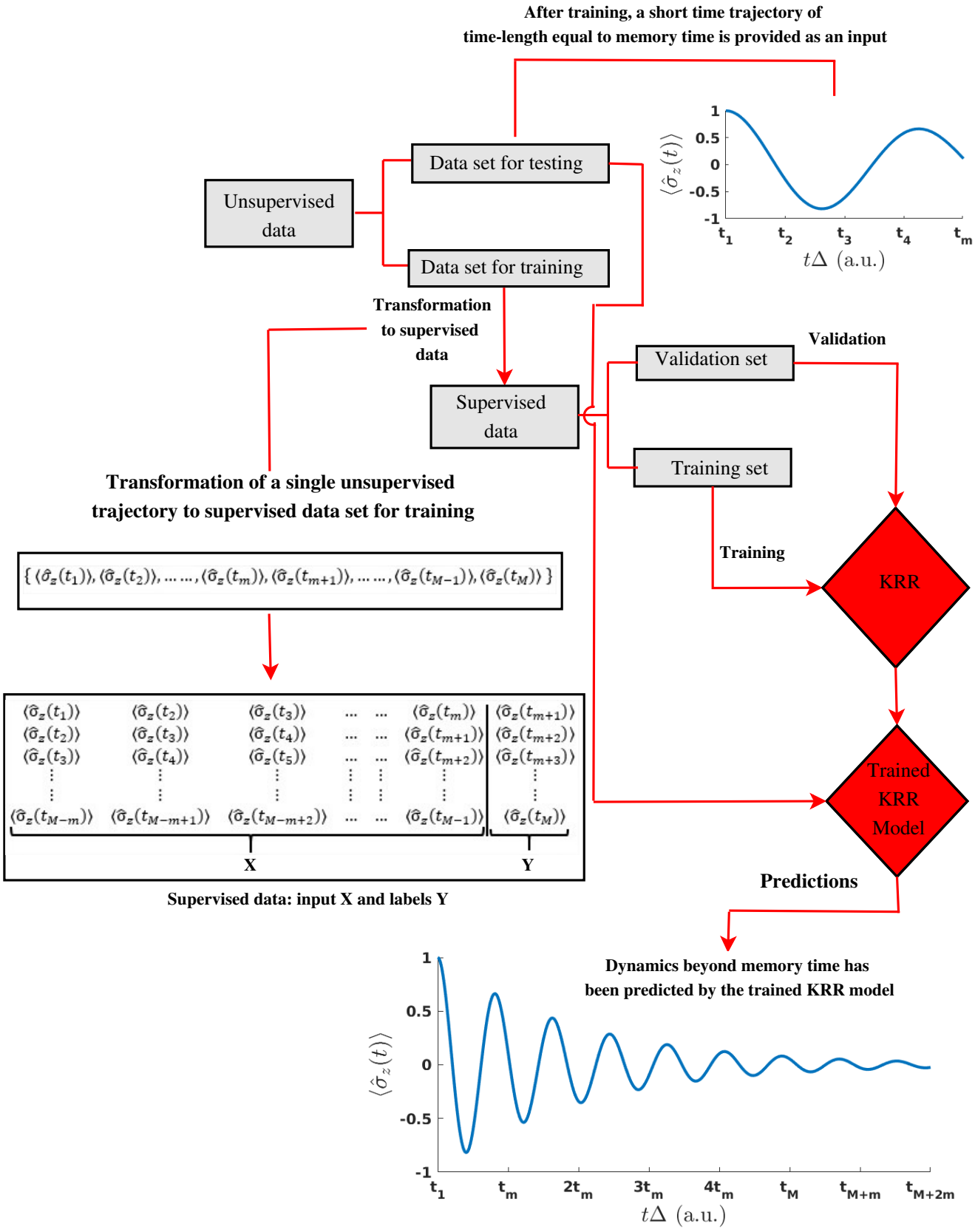

Figure 1: Flowchart of all steps during data preparation, training and predictions.

by excluding the first point and appending the $\langle\hat{\sigma}_z\rangle$ value at t_{m+1} to form the next input vector $\mathbf{x}_2$. Now we take the value $\langle\hat{\sigma}_z\rangle$ at t_{m+2} as a target output value y_2. This process continues till time-step t_M as shown schematically in Fig. 1. In our case, we took $t_m = 4$ and $\Delta t_{train} = 0.1$ resulting in $N = (t_M - t_m)/\Delta t_{train} = (20 - 4)/0.1 = 160$ supervised data points from each trajectory.

From the data set of 1000 trajectories, 100 randomly chosen trajectories are taken as the hold-out test set, which we use testing our approach and the results presented in this paper are shown for this hold-out set. With $\Delta t_{\text{train}} = 0.1$ and $t_m = 4$, the remaining set of 900 unsupervised trajectories of time-length $t_M = 20$ are transformed into 144000 supervised trajectories of time-length $t_m = 4$. The data set of supervised trajectories is randomly partitioned into two subsets: a training set, which contains 80% of the data and a validation set with 20% random trajectories of the set (see Fig. 1) for the optimization of hyperparameters σ and λ on the logarithmic grid.[98] For ML calculations we used the MLatom package[98–100] (training data and input files for MLatom can be found at https://doi.org/10.6084/m9.figshare.15134649 as described in Data and Code Availability section). Since the cost of training a KRR model scales as N^3, instead of training a single model, we reduced the training cost by training two separate models for symmetric and asymmetric cases, which halves the number of training points. The training for each case takes $\approx$ 8.20 hrs with parallel computation on 36 Intel(R) Xeon(R) Gold 6240 CPUs @ 2.60GHz.

Results and Discussion

After training our KRR model, it uses as input vector $\mathbf{x}$, $\langle\hat{\sigma}_z\rangle$ values taken with the step Δt_{train} from the short-time trajectory run with the HEOM up to the memory time t_m and predicts the value $\langle\hat{\sigma}_z\rangle$ at the next time step t_{m+1}. We prepare a new input vector by removing the first point and appending the $\langle\hat{\sigma}_z\rangle$ value at t_{m+1} and predict with KRR the $\langle\hat{\sigma}_z\rangle$ at the next time step t_{m+2}. This process continues until trajectory reaches final

Table 1: Mean absolute error (MAE), mean square error (MSE) and root mean square error (RMSE) for the hold-out test set of 100 trajectories within time-window 4-20.

SB models	MAE	MSE	RMSE
Symmetric	9.20×10^{-4}	6.12×10^{-6}	2.47×10^{-3}
Asymmetric	1.97×10^{-3}	8.00×10^{-5}	8.94×10^{-3}

run time t_M. This way, KRR uses short-time HEOM trajectories run up to the memory time t_m to predict long-time trajectories run up to time t_M and beyond (see Fig. 1; the code, ML models, and necessary data for running dynamics with MLatom can be found at https://doi.org/10.6084/m9.figshare.15134649 as described in Data and Code Availability section; it is worth emphasising that the fed short-time input trajectories are unseen to our trained KRR models). This approach gives us the valuable information about the temporal evolution of the state population in contrast to alternative approaches, where ML was used to completely bypass HEOM dynamics and predict the final properties of interest such as transfer times and transfer efficiencies in the pigment–protein complexes.[103]

Fig. 2 shows results for symmetric SB model with a wide range of parameters. Similarly, Fig. 3 shows results for asymmetric SB model. Noteworthy, our KRR model can faithfully reproduce the reference HEOM trajectories at least up to run time $t_M = 30$ as we show in Figs. 2 and 3, which means that KRR is capable of extrapolating beyond the time-limit $t_M = 20$ used for training. Fig. 2 and Fig. 3 show small fraction of results. For the remaining results of the hold-out test set, interested readers are referred to the Supporting Information (In the Supporting information, the trajectories are propagated up-to $t_M = 20$). The predicted results cover a wide range of scenarios from strong environment to weak environment and from strong coupling to weak coupling. The errors for the hold-out test set of 100 trajectories are shown in Table 1.

From Fig. 2, we can see that the predictions by KRR model are very accurate for symmetric cases. For asymmetric SB model, the predicted result given in Fig. S3-(3f) of the Supporting Information slightly deviate from the the exact HEOM results in the long-time regime. The possible reason is that the memory-time or in other words, the window-size of

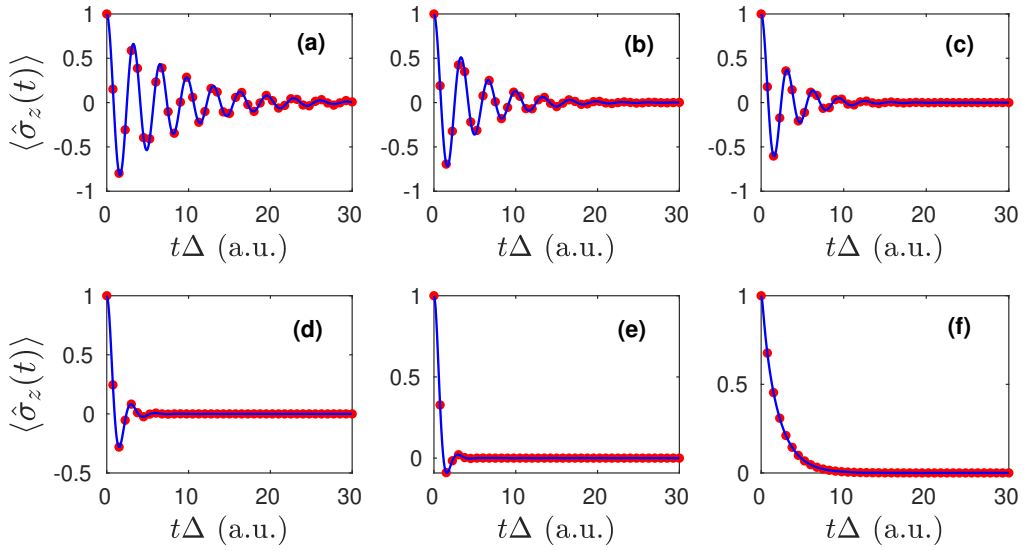

Figure 2: Expectation value of $\hat{\sigma}_z$ for symmetric SB model (i.e., $\epsilon = 0.0$) as a function of time. Results predicted by KRR model (blue line) are compared to the HEOM results (red dots). The adopted parameters are: (a) $\eta = 0.2$, $\omega_c = 8.0$, $\beta = 1.0$; (b) $\eta = 0.4$, $\omega_c = 10.0$, $\beta = 1.0$; (c) $\eta = 0.2$, $\omega_c = 10.0$, $\beta = 0.25$; (d) $\eta = 0.1$, $\omega_c = 4.0$, $\beta = 0.1$; (e) $\eta = 0.8$, $\omega_c = 3.0$, $\beta = 1.0$; (f) $\eta = 1.0$, $\omega_c = 2.0$, $\beta = 0.1$. Here $\Delta = 1.0$ and on x-axis t is multiplied by Δ, following Ref. 104. All parameters are in atomic units.

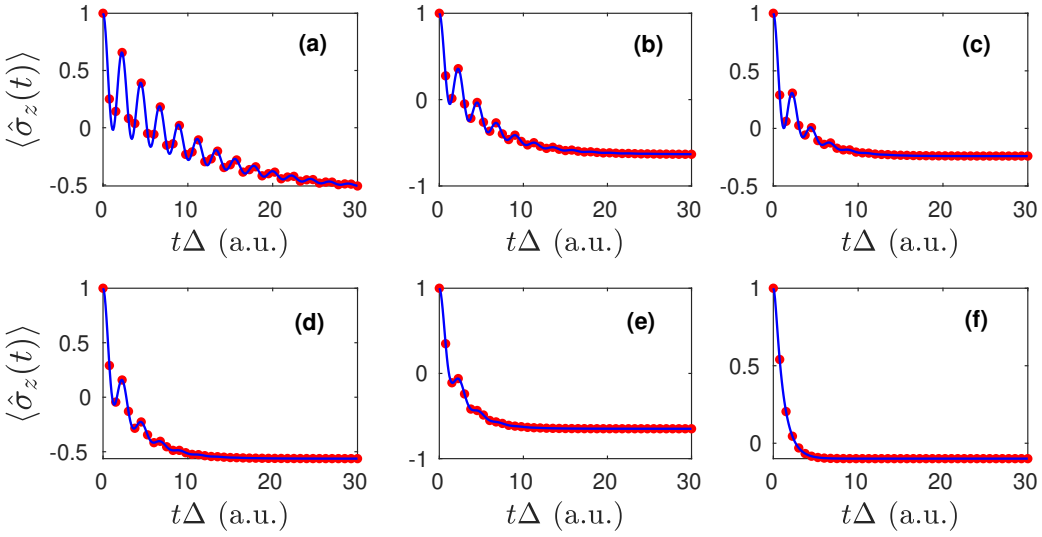

Figure 3: Expectation value of $\hat{\sigma}_z$ for asymmetric SB model (i.e., $\epsilon = 1.0$) as a function of time. Results predicted by KRR model (blue line) are compared to the HEOM results (red dots). The adopted parameters are: (a) $\eta = 0.1$, $\omega_c = 6.0$, $\beta = 0.75$; (b) $\eta = 0.3$, $\omega_c = 8.0$, $\beta = 1.0$; (c) $\eta = 0.2$, $\omega_c = 10.0$, $\beta = 0.25$; (d) $\eta = 0.4$, $\omega_c = 8.0$, $\beta = 0.75$; (e) $\eta = 0.8$, $\omega_c = 10.0$, $\beta = 1.0$; (f) $\eta = 0.7$, $\omega_c = 10.0$, $\beta = 0.1$. Here $\Delta = 1.0$ and on x-axis t is multiplied by Δ, following Ref. 104. All parameters are in atomic units.

the base trajectory ($|0-t_m|$) is not enough for this case. In this work, we have considered the same memory time for both symmetric and asymmetric SB models, but it is advised to train separate models for symmetric and asymmetric SB cases with different memory times. The accuracy of the KRR model depends on memory time. By increasing the memory time, the KRR model gets more accurate in the predictions as shown for the hold-out trajectories in Fig. 4. The window-size of the base trajectory ($|0-t_m|$) should be wide enough, so that ML model can learn to differentiate among different trajectories. For not wide enough window-size, KRR model cannot differentiate well between two input trajectories, which results in a rapid deterioration of the accuracy.

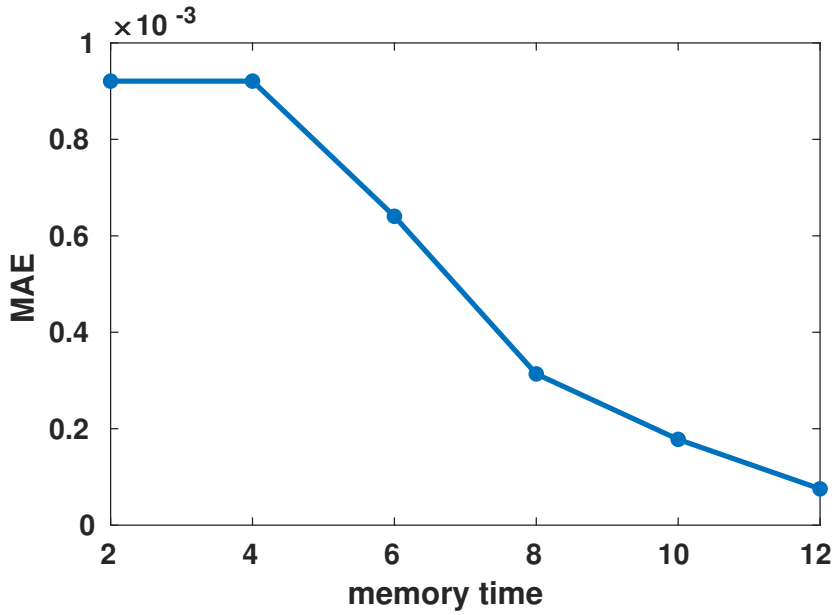

Figure 4: Mean absolute error (MAE) as a function of memory time t_m. The MAE is averaged over 50 hold-out symmetric trajectories for the time-window t =12–20.

As predicted value is included in the input for the next time step, the error accumulation with time is inevitable, which imposes strict requirements on the accuracy of the predictions as for less accurate ML models the quality of trajectories will rapidly deteriorate. Fig. S5 of Supporting Information shows the increase of absolute error in the predictions with the passage of time for the deviating trajectory Fig. S3-(3f) of Supporting Information. As KRR is a nonparametric ML model, the number of parameters increases with the increase of

training points, which makes the training very time consuming and requires large memory. To avoid this problem, we should keep the number of points in the training set as minimum as possible. It can be done by using farthest-point sampling,[99] while choosing trajectories for training, or setting Δt_{train} to larger values while ensuring that it will not decrease the accuracy of the KRR predictions too much.

The computational cost-saving by our ML approach is substantial. The amount of time saving depends on the memory time and the trajectory time and in our case it is ca. 90%. This reduction in computational time may allow longer simulations with HEOM model at low temperatures, where its cost and memory requirements increase very fast. In contrast, after training, the computational cost of our KRR model remains the same for all cases. On a single Intel(R) Core(TM) i7-10700 CPU @ 2.90 GHz, prediction of the whole trajectory beyond the initial memory time t_m takes $\approx$2 min. In the future, our approach can be combined with SEOM, which requires a large number of trajectories to have good convergence in the long-time regime. After generating short time trajectory of time-length t_m with SEOM, our approach can be used to predict the long-time dynamics saving a tremendous amount of computational cost, which is currently the topic of our investigations.

Concluding Remarks

In this article, we have developed an ML approach to study quantum dissipative dynamics. We have demonstrated the ability of kernel ridge regression (KRR) to learn from relatively small amount of training data and predict the long-time quantum dissipative dynamics for two-level SB model without much loss of accuracy. After training, the KRR model requires short-time trajectory as input and as an output, it gives the dynamics for future times. The ability of predictions for future time makes KRR model or in general ML an appealing approach to avoid the calculation of expensive long-time dynamics. It can be combined with other approaches such as SEOM, which has bad convergence in long-time regime. Here,

we have only demonstrated results for the two-level SB model, but our approach can be extended to multi-level systems given that the data for training is provided. In the end, with the establishment of the database with the dynamics data, the ML approach has great potential to become a useful low-cost computational tool for studying the quantum dissipative dynamics.

Acknowledgement

POD acknowledges funding by the National Natural Science Foundation of China (No. 22003051) and via the Lab project of the State Key Laboratory of Physical Chemistry of Solid Surfaces. The authors thank Alexei A. Kananenka for clarifying his approach.

Supporting Information

Additional plots for the test trajectories.

Author Contributions

AU conceived the project, performed all the implementations, simulations, and analysis of the data, as well as written the original version of the manuscript. Both authors carried out the method development, discussed the results, and revised the manuscript. POD acquired funding for the project.

Data and Code Availability

The data and code are available at https://doi.org/10.6084/m9.figshare.15134649.

References

(1) Shor, P. W. Scheme for reducing decoherence in quantum computer memory. *Physical review A* **1995**, *52*, R2493.

(2) Pastawski, F.; Clemente, L.; Cirac, J. I. Quantum memories based on engineered dissipation. *Physical Review A* **2011**, *83*, 012304.

(3) Wen, X. Quantum Field Theory of Many-Body Systems, Oxford Graduate Texts. 2004.

(4) Le Hur, K.; Henriet, L.; Herviou, L.; Plekhanov, K.; Petrescu, A.; Goren, T.; Schiro, M.; Mora, C.; Orth, P. P. Driven dissipative dynamics and topology of quantum impurity systems. *Comptes Rendus Physique* **2018**, *19*, 451–483.

(5) Wurfel, U.; Thorwart, M.; Weber, E. R. *Quantum Efficiency in Complex Systems, Part II: From Molecular Aggregates to: Organic Solar Cells*; Academic Press, 2011.

(6) Milošević, M.; Geurts, R. The Ginzburg–Landau theory in application. *Physica C: Superconductivity* **2010**, *470*, 791–795.

(7) Huelga, S. F.; Plenio, M. B. Vibrations, quanta and biology. *Contemporary Physics* **2013**, *54*, 181–207.

(8) Daley, A. J. Quantum trajectories and open many-body quantum systems. *Advances in Physics* **2014**, *63*, 77–149.

(9) Ji, W.; Xu, H.-Q.; Guo, H. Quantum description of transport phenomena: Recent progress. 2014.

(10) Hughes, K. H. *Dynamics of open quantum systems*; Collaborative Computational Project on Molecular Quantum Dynamics (CCP6), 2006.

(11) Golding, B.; Zimmerman, M. N.; Coppersmith, S. Dissipative quantum tunneling of a single microscopic defect in a mesoscopic metal. *Physical review letters* **1992**, *68*, 998.

(12) Vojta, M.; Bulla, R. Kondo effect of impurity moments in d-wave superconductors: Quantum phase transition and spectral properties. *Physical Review B* **2001**, *65*, 014511.

(13) Del Valle, E.; Zippilli, S.; Laussy, F. P.; Gonzalez-Tudela, A.; Morigi, G.; Tejedor, C. Two-photon lasing by a single quantum dot in a high-Q microcavity. *Physical Review B* **2010**, *81*, 035302.

(14) Ota, Y.; Iwamoto, S.; Kumagai, N.; Arakawa, Y. Spontaneous two-photon emission from a single quantum dot. *Physical review letters* **2011**, *107*, 233602.

(15) Reed, M. D.; DiCarlo, L.; Nigg, S. E.; Sun, L.; Frunzio, L.; Girvin, S. M.; Schoelkopf, R. J. Realization of three-qubit quantum error correction with superconducting circuits. *Nature* **2012**, *482*, 382–385.

(16) Georgescu, I. Trapped ion quantum computing turns 25. *Nature Reviews Physics* **2020**, *2*, 278–278.

(17) Wilson, K. G. The renormalization group: Critical phenomena and the Kondo problem. *Reviews of modern physics* **1975**, *47*, 773.

(18) Bulla, R.; Tong, N.-H.; Vojta, M. Numerical renormalization group for bosonic systems and application to the sub-ohmic spin-boson model. *Physical review letters* **2003**, *91*, 170601.

(19) White, S. R. Density matrix formulation for quantum renormalization groups. *Physical review letters* **1992**, *69*, 2863.

(20) Wong, H.; Chen, Z.-D. Density matrix renormalization group approach to the spin-boson model. *Physical Review B* **2008**, *77*, 174305.

(21) Egger, R.; Weiss, U. Quantum Monte Carlo simulation of the dynamics of the spin-boson model. *Zeitschrift für Physik B Condensed Matter* **1992**, *89*, 97–107.

(22) Winter, A.; Rieger, H.; Vojta, M.; Bulla, R. Quantum phase transition in the sub-ohmic spin-boson model: Quantum monte carlo study with a continuous imaginary time cluster algorithm. *Physical review letters* **2009**, *102*, 030601.

(23) Chin, A. W.; Rivas, Á.; Huelga, S. F.; Plenio, M. B. Exact mapping between system-reservoir quantum models and semi-infinite discrete chains using orthogonal polynomials. *Journal of Mathematical Physics* **2010**, *51*, 092109.

(24) Prior, J.; Chin, A. W.; Huelga, S. F.; Plenio, M. B. Efficient simulation of strong system-environment interactions. *Physical review letters* **2010**, *105*, 050404.

(25) Puebla, R.; Zicari, G.; Arrazola, I.; Solano, E.; Paternostro, M.; Casanova, J. Spin-boson model as a simulator of non-Markovian multiphoton Jaynes-Cummings models. *Symmetry* **2019**, *11*, 695.

(26) Meyer, H.-D.; Manthe, U.; Cederbaum, L. S. The multi-configurational time-dependent Hartree approach. *Chemical Physics Letters* **1990**, *165*, 73–78.

(27) Wang, H.; Thoss, M. A multilayer multiconfiguration time-dependent Hartree simulation of the reaction-coordinate spin-boson model employing an interaction picture. *The Journal of chemical physics* **2017**, *146*, 124112.

(28) Wang, H.; Thoss, M. Multilayer formulation of the multiconfiguration time-dependent Hartree theory. *The Journal of chemical physics* **2003**, *119*, 1289–1299.

(29) Nakajima, S. On quantum theory of transport phenomena: steady diffusion. *Progress of Theoretical Physics* **1958**, *20*, 948–959.

(30) Zwanzig, R. Ensemble method in the theory of irreversibility. *The Journal of Chemical Physics* **1960**, *33*, 1338–1341.

(31) Cerrillo, J.; Cao, J. Non-Markovian dynamical maps: numerical processing of open quantum trajectories. *Physical review letters* **2014**, *112*, 110401.

(32) Kananenka, A. A.; Hsieh, C.-Y.; Cao, J.; Geva, E. Accurate Long-Time Mixed Quantum-Classical Liouville Dynamics via the Transfer Tensor Method. *The journal of physical chemistry letters* **2016**, *7*, 4809–4814.

(33) Buser, M.; Cerrillo, J.; Schaller, G.; Cao, J. Initial system-environment correlations via the transfer-tensor method. *Physical Review A* **2017**, *96*, 062122.

(34) Zhou, N.; Zhang, Y.; Lü, Z.; Zhao, Y. Variational Study of the Two-Impurity Spin–Boson Model with a Common Ohmic Bath: Ground-State Phase Transitions. *Annalen der Physik* **2018**, *530*, 1800120.

(35) Miller, W. H.; Cotton, S. J. Classical molecular dynamics simulation of electronically non-adiabatic processes. *Faraday discussions* **2017**, *195*, 9–30.

(36) Cotton, S. J.; Miller, W. H. The symmetrical quasi-classical model for electronically non-adiabatic processes applied to energy transfer dynamics in site-exciton models of light-harvesting complexes. *Journal of chemical theory and computation* **2016**, *12*, 983–991.

(37) Cotton, S. J.; Miller, W. H. A symmetrical quasi-classical windowing model for the molecular dynamics treatment of non-adiabatic processes involving many electronic states. *The Journal of chemical physics* **2019**, *150*, 104101.

(38) Meyer, H.-D.; Miller, W. H. Classical models for electronic degrees of freedom: Derivation via spin analogy and application to F*+ H2→ F+ H2. *The Journal of Chemical Physics* **1979**, *71*, 2156–2169.

(39) Stock, G.; Thoss, M. Semiclassical description of nonadiabatic quantum dynamics. *Physical review letters* **1997**, *78*, 578.

(40) Runeson, J. E.; Richardson, J. O. Generalized spin mapping for quantum-classical dynamics. *The Journal of chemical physics* **2020**, *152*, 084110.

(41) Mannouch, J. R.; Richardson, J. O. A partially linearized spin-mapping approach for nonadiabatic dynamics. I. Derivation of the theory. *The Journal of Chemical Physics* **2020**, *153*, 194109.

(42) Makarov, D. E.; Makri, N. Path integrals for dissipative systems by tensor multiplication. Condensed phase quantum dynamics for arbitrarily long time. *Chemical physics letters* **1994**, *221*, 482–491.

(43) Makri, N. Numerical path integral techniques for long time dynamics of quantum dissipative systems. *Journal of Mathematical Physics* **1995**, *36*, 2430–2457.

(44) Yan, Y.-a.; Yang, F.; Liu, Y.; Shao, J. Hierarchical approach based on stochastic decoupling to dissipative systems. *Chemical physics letters* **2004**, *395*, 216–221.

(45) Tanimura, Y. Stochastic Liouville, Langevin, Fokker–Planck, and master equation approaches to quantum dissipative systems. *Journal of the Physical Society of Japan* **2006**, *75*, 082001.

(46) Jin, J.; Zheng, X.; Yan, Y. Exact dynamics of dissipative electronic systems and quantum transport: Hierarchical equations of motion approach. *The Journal of chemical physics* **2008**, *128*, 234703.

(47) Shi, Q.; Chen, L.; Nan, G.; Xu, R.-X.; Yan, Y. Efficient hierarchical Liouville space propagator to quantum dissipative dynamics. *The Journal of chemical physics* **2009**, *130*, 084105.

(48) Hu, J.; Xu, R.-X.; Yan, Y. Communication: Padé spectrum decomposition of Fermi function and Bose function. 2010.

(49) Liu, H.; Zhu, L.; Bai, S.; Shi, Q. Reduced quantum dynamics with arbitrary bath spectral densities: Hierarchical equations of motion based on several different bath decomposition schemes. *The Journal of chemical physics* **2014**, *140*, 134106.

(50) Gong, H.; Ullah, A.; Ye, L.; Zheng, X.; Yan, Y. Quantum entanglement of parallel-coupled double quantum dots: A theoretical study using the hierarchical equations of motion approach. *Chinese Journal of Chemical Physics* **2018**, *31*, 510.

(51) Han, L.; Zhang, H.-D.; Zheng, X.; Yan, Y. On the exact truncation tier of fermionic hierarchical equations of motion. *The Journal of chemical physics* **2018**, *148*, 234108.

(52) Cui, L.; Zhang, H.-D.; Zheng, X.; Xu, R.-X.; Yan, Y. Highly efficient and accurate sum-over-poles expansion of Fermi and Bose functions at near zero temperatures: Fano spectrum decomposition scheme. *The Journal of chemical physics* **2019**, *151*, 024110.

(53) Zhang, H.-D.; Cui, L.; Gong, H.; Xu, R.-X.; Zheng, X.; Yan, Y. Hierarchical equations of motion method based on Fano spectrum decomposition for low temperature environments. *The Journal of chemical physics* **2020**, *152*, 064107.

(54) Tanimura, Y.; Kubo, R. Time evolution of a quantum system in contact with a nearly Gaussian-Markoffian noise bath. *Journal of the Physical Society of Japan* **1989**, *58*, 101–114.

(55) Stockburger, J. T.; Mak, C. Dynamical simulation of current fluctuations in a dissipative two-state system. *Physical review letters* **1998**, *80*, 2657.

(56) Stockburger, J. T.; Grabert, H. Non-Markovian quantum state diffusion. *Chemical Physics* **2001**, *268*, 249–256.

(57) Stockburger, J. T.; Grabert, H. Exact c-number representation of non-Markovian quantum dissipation. *Physical review letters* **2002**, *88*, 170407.

(58) Stockburger, J. T. Simulating spin-boson dynamics with stochastic liouville–von neumann equations. *Chemical physics* **2004**, *296*, 159–169.

(59) Koch, W.; Großmann, F.; Stockburger, J. T.; Ankerhold, J. Non-Markovian dissipative semiclassical dynamics. *Physical review letters* **2008**, *100*, 230402.

(60) Stockburger, J. T. Exact propagation of open quantum systems in a system-reservoir context. *EPL (Europhysics Letters)* **2016**, *115*, 40010.

(61) Schmitz, K.; Stockburger, J. T. A variance reduction technique for the stochastic Liouville–von Neumann equation. *The European Physical Journal Special Topics* **2019**, *227*, 1929–1937.

(62) Shao, J. Decoupling quantum dissipation interaction via stochastic fields. *The Journal of chemical physics* **2004**, *120*, 5053–5056.

(63) Zhou, Y.; Yan, Y.; Shao, J. Stochastic simulation of quantum dissipative dynamics. *EPL (Europhysics Letters)* **2005**, *72*, 334.

(64) Shao, J. Rigorous representation and exact simulation of real Gaussian stationary processes. *Chemical Physics* **2010**, *375*, 378–379.

(65) Hsieh, C.-Y.; Cao, J. A unified stochastic formulation of dissipative quantum dynamics. II. Beyond linear response of spin baths. *The Journal of chemical physics* **2018**, *148*, 014104.

(66) McCaul, G.; Lorenz, C.; Kantorovich, L. Partition-free approach to open quantum systems in harmonic environments: An exact stochastic Liouville equation. *Physical Review B* **2017**, *95*, 125124.

(67) Ke, Y.; Zhao, Y. Hierarchy of forward-backward stochastic Schrödinger equation. *The Journal of chemical physics* **2016**, *145*, 024101.

(68) Ke, Y.; Zhao, Y. An extension of stochastic hierarchy equations of motion for the equilibrium correlation functions. *The Journal of chemical physics* **2017**, *146*, 214105.

(69) Han, L.; Ullah, A.; Yan, Y.-A.; Zheng, X.; Yan, Y.; Chernyak, V. Stochastic equation of motion approach to fermionic dissipative dynamics. I. Formalism. *The Journal of Chemical Physics* **2020**, *152*, 204105.

(70) Ullah, A.; Han, L.; Yan, Y.-A.; Zheng, X.; Yan, Y.; Chernyak, V. Stochastic equation of motion approach to fermionic dissipative dynamics. II. Numerical implementation. *The Journal of Chemical Physics* **2020**, *152*, 204106.

(71) Han, L.; Chernyak, V.; Yan, Y.-A.; Zheng, X.; Yan, Y. Stochastic Representation of Non-Markovian Fermionic Quantum Dissipation. *Physical review letters* **2019**, *123*, 050601.

(72) Zhong, X.; Zhao, Y. Non-Markovian stochastic Schrödinger equation at finite temperatures for charge carrier dynamics in organic crystals. *The Journal of chemical physics* **2013**, *138*, 014111.

(73) Wang, Y.-C.; Ke, Y.; Zhao, Y. The hierarchical and perturbative forms of stochastic Schrödinger equations and their applications to carrier dynamics in organic materials. *Wiley Interdisciplinary Reviews: Computational Molecular Science* **2019**, *9*, e1375.

(74) Lian, M.; Wang, Y.-C.; Ke, Y.; Zhao, Y. Non-Markovian stochastic Schrödinger equation in k-space toward the calculation of carrier dynamics in organic semiconductors. *The Journal of chemical physics* **2019**, *151*, 044115.

(75) Wang, Y.-C.; Zhao, Y. The hierarchical stochastic Schrödinger equations: Theory and applications. *Chinese Journal of Chemical Physics* **2020**, *33*, 653–667.

(76) Dral, P. O. Quantum chemistry assisted by machine learning. *Advances in Quantum Chemistry* **2020**, *81*, 291–324.

(77) von Lilienfeld, O. A.; Müller, K.-R.; Tkatchenko, A. Exploring chemical compound space with quantum-based machine learning. *Nat. Rev. Chem.* **2020**, *4*, 347–358.

(78) Unke, O. T.; Chmiela, S.; Sauceda, H. E.; Gastegger, M.; Poltavsky, I.; Schutt, K. T.; Tkatchenko, A.; Muller, K. R. Machine Learning Force Fields. *Chem. Rev.* **2021**, DOI: 10.1021/acs.chemrev.0c01111.

(79) Manzhos, S.; Carrington, J., T. Neural Network Potential Energy Surfaces for Small Molecules and Reactions. *Chem. Rev.* **2020**, DOI: 10.1021/acs.chemrev.0c00665.

(80) Wang, J.; Chmiela, S.; Müller, K.-R.; Noé, F.; Clementi, C. Ensemble learning of coarse-grained molecular dynamics force fields with a kernel approach. *The Journal of Chemical Physics* **2020**, *152*, 194106.

(81) Veit, M.; Wilkins, D. M.; Yang, Y.; DiStasio Jr, R. A.; Ceriotti, M. Predicting molecular dipole moments by combining atomic partial charges and atomic dipoles. *The Journal of Chemical Physics* **2020**, *153*, 024113.

(82) Morita, K.; Davies, D. W.; Butler, K. T.; Walsh, A. Modeling the dielectric constants of crystals using machine learning. *The Journal of Chemical Physics* **2020**, *153*, 024503.

(83) Xue, B.-X.; Barbatti, M.; Dral, P. O. Machine Learning for Absorption Cross Sections. *The Journal of Physical Chemistry A* **2020**, *124*, 7199–7210.

(84) Dral, P. O.; Barbatti, M. Molecular excited states through a machine learning lens. *Nature Reviews Chemistry* **2021**, 1–18.

(85) Westermayr, J.; Marquetand, P. Machine learning and excited-state molecular dynamics. *Mach. Learn.: Sci. Technol.* **2020**, *1*, 043001.

(86) Ueno, S.; Tanimura, Y. Modeling and simulating the excited-state dynamics of a system with condensed phases: A machine learning approach. *Journal of Chemical Theory and Computation* **2021**,

(87) Yang, B.; He, B.; Wan, J.; Kubal, S.; Zhao, Y. Applications of neural networks to dynamics simulation of Landau-Zener transitions. *Chemical Physics* **2020**, *528*, 110509.

(88) Bandyopadhyay, S.; Huang, Z.; Sun, K.; Zhao, Y. Applications of neural networks to

the simulation of dynamics of open quantum systems. *Chemical Physics* **2018**, *515*, 272–278.

(89) Herrera Rodríguez, L. E.; Kananenka, A. A. Convolutional Neural Networks for Long Time Dissipative Quantum Dynamics. *The Journal of Physical Chemistry Letters* **2021**, *12*, 2476–2483.

(90) Lin, K.; Peng, J.; Gu, F. L.; Lan, Z. Simulation of Open Quantum Dynamics with Bootstrap-Based Long Short-Term Memory Recurrent Neural Network. *arXiv preprint arXiv:2108.01310* **2021**,

(91) Kamath, A.; Vargas-Hernández, R. A.; Krems, R. V.; Carrington, J., T.; Manzhos, S. Neural networks vs Gaussian process regression for representing potential energy surfaces: A comparative study of fit quality and vibrational spectrum accuracy. *J. Chem. Phys.* **2018**, *148*, 241702.

(92) Nguyen, T. T.; Szekely, E.; Imbalzano, G.; Behler, J.; Csányi, G.; Ceriotti, M.; Gotz, A. W.; Paesani, F. Comparison of permutationally invariant polynomials, neural networks, and Gaussian approximation potentials in representing water interactions through many-body expansions. *J. Chem. Phys.* **2018**, *148*, 241725.

(93) Hansen, K.; Montavon, G.; Biegler, F.; Fazli, S.; Rupp, M.; Scheffler, M.; von Lilienfeld, O. A.; Tkatchenko, A.; Müller, K.-R. Assessment and Validation of Machine Learning Methods for Predicting Molecular Atomization Energies. *J. Chem. Theory Comput.* **2013**, *9*, 3404–3419.

(94) Pinheiro Jr, M.; Ge, F.; Ferré, N.; Dral, P. O.; Barbatti, M. Choosing the right molecular machine learning potential. *Chem. Sci.* **2021**, *accepted*.

(95) Stulp, F.; Sigaud, O. Many regression algorithms, one unified model: A review. *Neural Networks* **2015**, *69*, 60–79.

(96) Hastie, T.; Tibshirani, R.; Friedman, J. The elements of statistical learning: Data mining, inference, and prediction. 2009.

(97) Rupp, M. Machine learning for quantum mechanics in a nutshell. *International Journal of Quantum Chemistry* **2015**, *115*, 1058–1073.

(98) Dral, P. O. MLatom: A program package for quantum chemical research assisted by machine learning. *Journal of computational chemistry* **2019**, *40*, 2339–2347.

(99) Dral, P. O.; Ge, F.; Xue, B.-X.; Hou, Y.-F.; Pinheiro, M.; Huang, J.; Barbatti, M. MLatom 2: An Integrative Platform for Atomistic Machine Learning. *Topics in Current Chemistry* **2021**, *379*, 1–41.

(100) Dral, P. O.; Xue, B.-X.; Ge, F.; Hou, Y.-F.; Pinheiro Jr, M. *MLatom*: a Package for Atomistic Simulations with Machine Learning. http://MLatom.com (accessed on August 9, 2021). Xiamen University: Xiamen, China, 2013–2021.

(101) Witten, I. H.; Frank, E.; Hall, M. A.; Pal, C.; DATA, M. Practical machine learning tools and techniques. DATA MINING. 2005; p 4.

(102) Johansson, J. R.; Nation, P. D.; Nori, F. QuTiP: An open-source Python framework for the dynamics of open quantum systems. *Computer Physics Communications* **2012**, *183*, 1760–1772.

(103) Häse, F.; Kreisbeck, C.; Aspuru-Guzik, A. Machine learning for quantum dynamics: deep learning of excitation energy transfer properties. *Chem. Sci.* **2017**, *8*, 8419–8426.

(104) He, X.; Liu, J. A new perspective for nonadiabatic dynamics with phase space mapping models. *The Journal of chemical physics* **2019**, *151*, 024105.

Supporting information for:

Speeding up quantum dissipative dynamics of open systems with kernel methods

Arif Ullah* and Pavlo O. Dral*

State Key Laboratory of Physical Chemistry of Solid Surfaces, Fujian Provincial Key Laboratory of Theoretical and Computational Chemistry, Department of Chemistry, and College of Chemistry and Chemical Engineering, Xiamen University, Xiamen 361005, China

E-mail: ua2024@xmu.edu.cn; dral@xmu.edu.cn

Table S1: Parameters for the sub-plots shown in Fig. S1-S4. The common parameter is $\Delta = 1.0$. All parameters are in atomic units (a.u.).

sub-plots	ϵ	λ	ω_c	β	sub-plots	ϵ	λ	ω_c	β
(1a)	0.0	0.1	1.0	0.5	(3a)	1.0	0.1	2.0	1.0
(1b)	0.0	0.1	1.0	0.25	(3b)	1.0	0.1	3.0	0.75
(1c)	0.0	0.1	4.0	0.75	(3c)	1.0	0.1	7.0	0.5
(1d)	0.0	0.1	6.0	0.5	(3d)	1.0	0.1	10.0	0.1
(1e)	0.0	0.2	1.0	0.75	(3e)	1.0	0.2	1.0	0.25
(1f)	0.0	0.2	3.0	0.5	(3f)	1.0	0.2	1.0	1.0
(1g)	0.0	0.2	7.0	1.0	(3g)	1.0	0.2	2.0	0.75
(1h)	0.0	0.3	1.0	0.25	(3h)	1.0	0.2	4.0	0.1

Continued on next page

Table S1 – *Continued from previous page*

sub-plots	ϵ	λ	ω_c	β	sub-plots	ϵ	λ	ω_c	β
(1i)	0.0	0.3	2.0	1.0	(3i)	1.0	0.2	4.0	0.5
(1j)	0.0	0.3	8.0	0.5	(3j)	1.0	0.2	5.0	0.75
(1k)	0.0	0.3	8.0	0.25	(3k)	1.0	0.2	6.0	1.0
(1l)	0.0	0.3	8.0	0.75	(3l)	1.0	0.2	7.0	0.25
(1m)	0.0	0.4	2.0	0.1	(3m)	1.0	0.2	8.0	0.5
(1n)	0.0	0.4	2.0	0.25	(3n)	1.0	0.2	8.0	0.25
(1o)	0.0	0.4	3.0	0.75	(3o)	1.0	0.3	2.0	0.25
(1p)	0.0	0.4	6.0	0.1	(3p)	1.0	0.3	4.0	1.0
(1q)	0.0	0.4	6.0	0.75	(3q)	1.0	0.3	7.0	0.25
(1r)	0.0	0.4	7.0	0.25	(3r)	1.0	0.3	8.0	0.75
(1s)	0.0	0.4	8.0	1.0	(3s)	1.0	0.3	10.0	1.0
(1t)	0.0	0.5	1.0	0.5	(3t)	1.0	0.4	2.0	0.75
(1u)	0.0	0.5	1.0	0.25	(3u)	1.0	0.4	7.0	0.1
(1v)	0.0	0.5	1.0	1.0	(3v)	1.0	0.4	7.0	1.0
(1w)	0.0	0.5	6.0	0.5	(3w)	1.0	0.5	1.0	0.5
(1x)	0.0	0.5	8.0	0.1	(3x)	1.0	0.5	3.0	0.5
(2a)	0.0	0.5	9.0	0.75	(4a)	1.0	0.5	8.0	0.25
(2b)	0.0	0.6	2.0	0.25	(4b)	1.0	0.5	8.0	0.75
(2c)	0.0	0.6	2.0	1.0	(4c)	1.0	0.6	1.0	0.1
(2d)	0.0	0.6	6.0	0.5	(4d)	1.0	0.6	1.0	1.0
(2e)	0.0	0.6	10.0	0.75	(4e)	1.0	0.6	4.0	1.0
(2f)	0.0	0.7	6.0	0.1	(4f)	1.0	0.7	1.0	0.75
(2g)	0.0	0.7	6.0	0.75	(4g)	1.0	0.7	5.0	0.25
(2h)	0.0	0.7	7.0	0.5	(4h)	1.0	0.7	6.0	0.5

Continued on next page

Table S1 – *Continued from previous page*

sub-plots	ϵ	λ	ω_c	β	sub-plots	ϵ	λ	ω_c	β
(2i)	0.0	0.7	7.0	0.25	(4i)	1.0	0.7	9.0	0.5
(2j)	0.0	0.7	8.0	0.1	(4j)	1.0	0.8	2.0	0.1
(2k)	0.0	0.7	8.0	0.75	(4k)	1.0	0.8	2.0	0.25
(2l)	0.0	0.7	9.0	0.1	(4l)	1.0	0.8	6.0	0.1
(2m)	0.0	0.9	4.0	0.5	(4m)	1.0	0.8	10.0	0.75
(2n)	0.0	0.9	10.0	1.0	(4n)	1.0	0.6	4.0	0.1
(2o)	0.0	1.0	5.0	0.75	(4o)	1.0	0.6	4.0	0.25
(2p)	0.0	1.0	6.0	0.25	(4p)	1.0	0.6	6.0	0.5
(2q)	0.0	1.0	8.0	0.5	(4q)	1.0	0.6	7.0	0.1
(2r)	0.0	1.0	8.0	1.0	(4r)	1.0	0.6	7.0	0.5
(2s)	0.0	1.0	9.0	0.1	(4s)	1.0	0.6	10.0	0.1
(2t)	0.0	1.0	10.0	0.1	(4t)	1.0	1.0	3.0	0.5

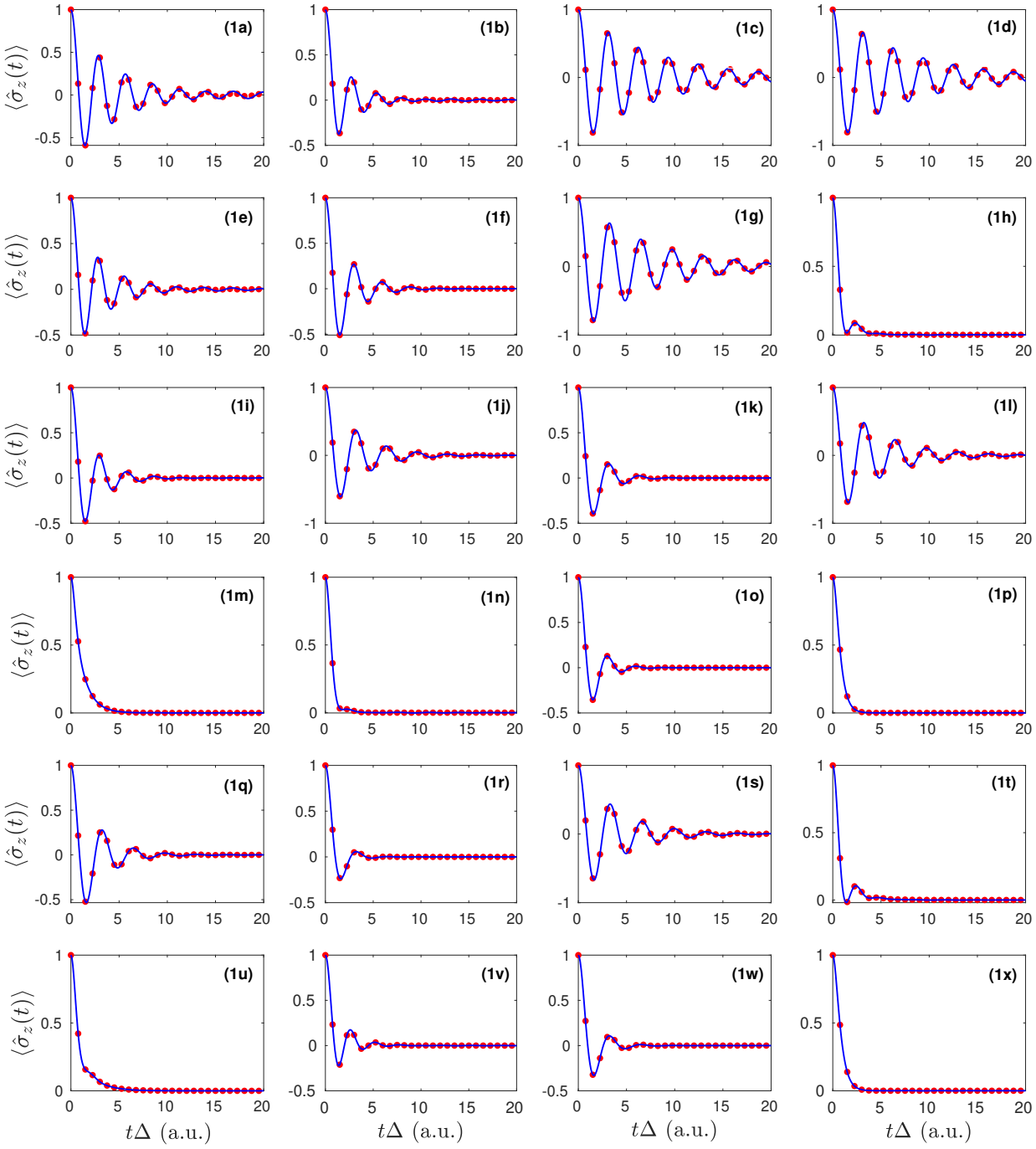

Figure S1: Expectation value of $\hat{\sigma}_z$ for symmetric SB model as a function of time. Results predicted by KRR model (blue line) are compared to the HEOM results (red dots). The adopted parameters are given in Table S1.

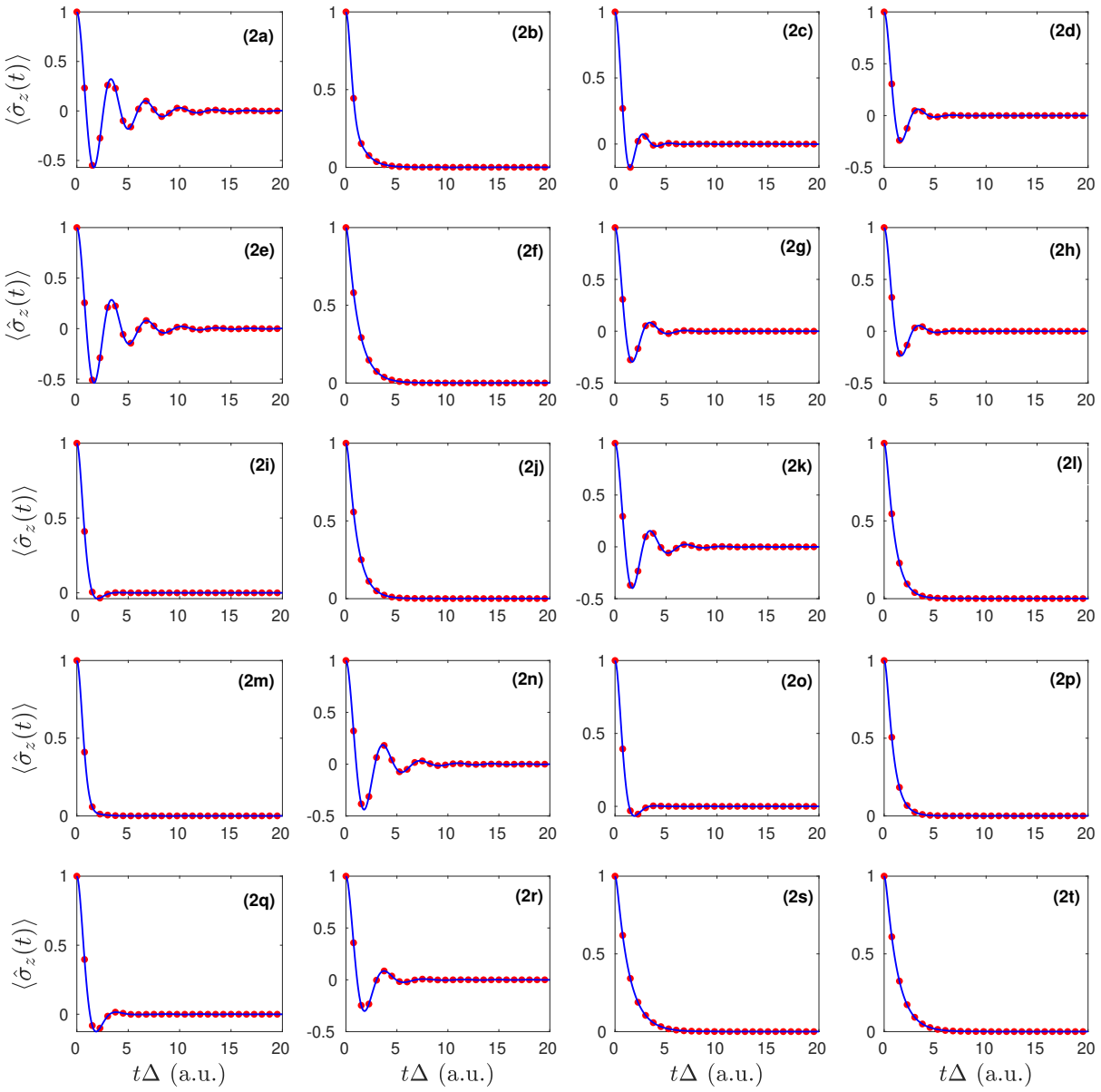

Figure S2: Expectation value of $\hat{\sigma}_z$ for symmetric SB model as a function of time. Results predicted by KRR model (blue line) are compared to the HEOM results (red dots). The adopted parameters are given in Table S1.

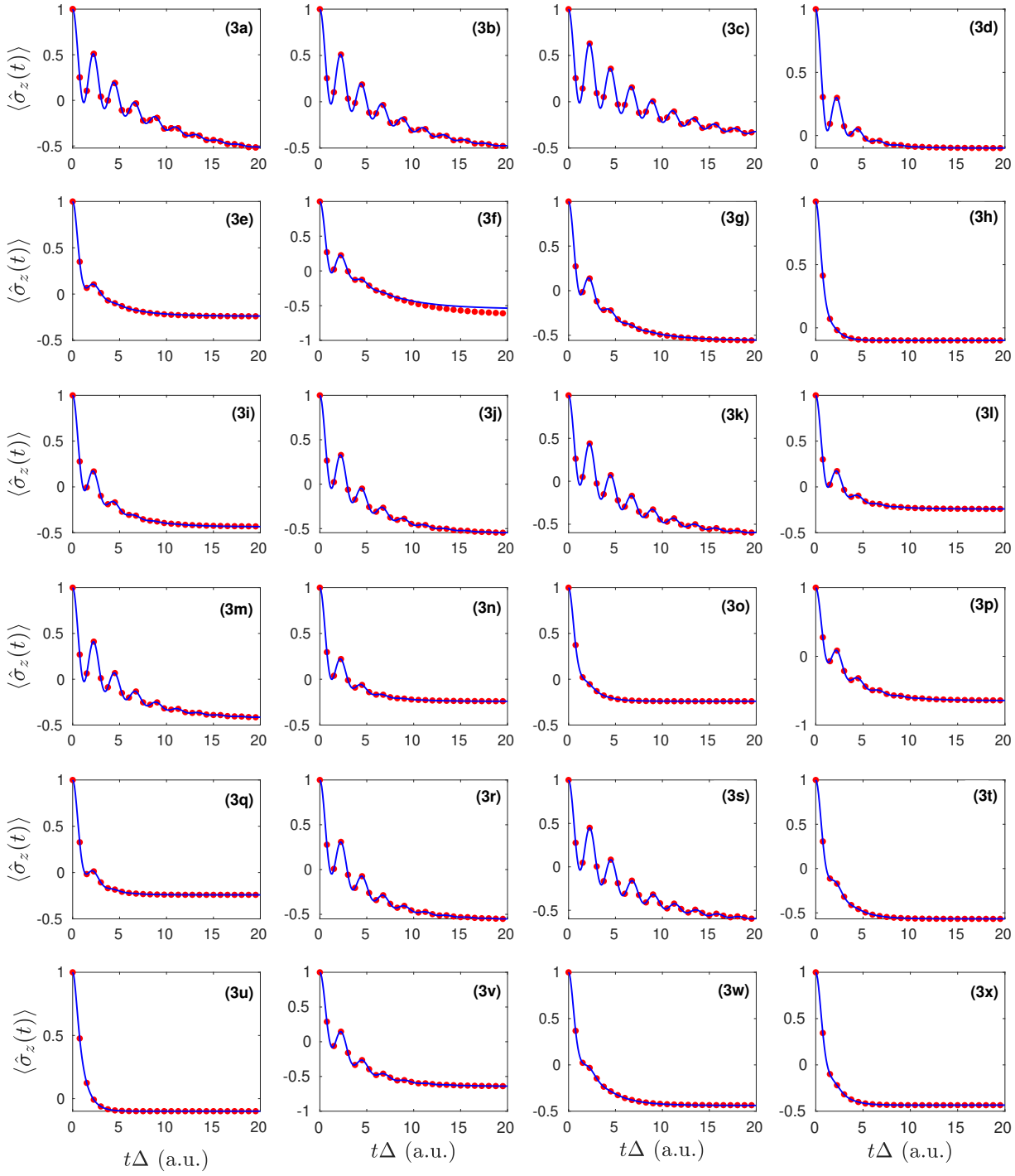

Figure S3: Expectation value of $\hat{\sigma}_z$ for asymmetric SB model as a function of time. Results predicted by KRR model (blue line) are compared to the HEOM results (red dots). The adopted parameters are given in Table S1.

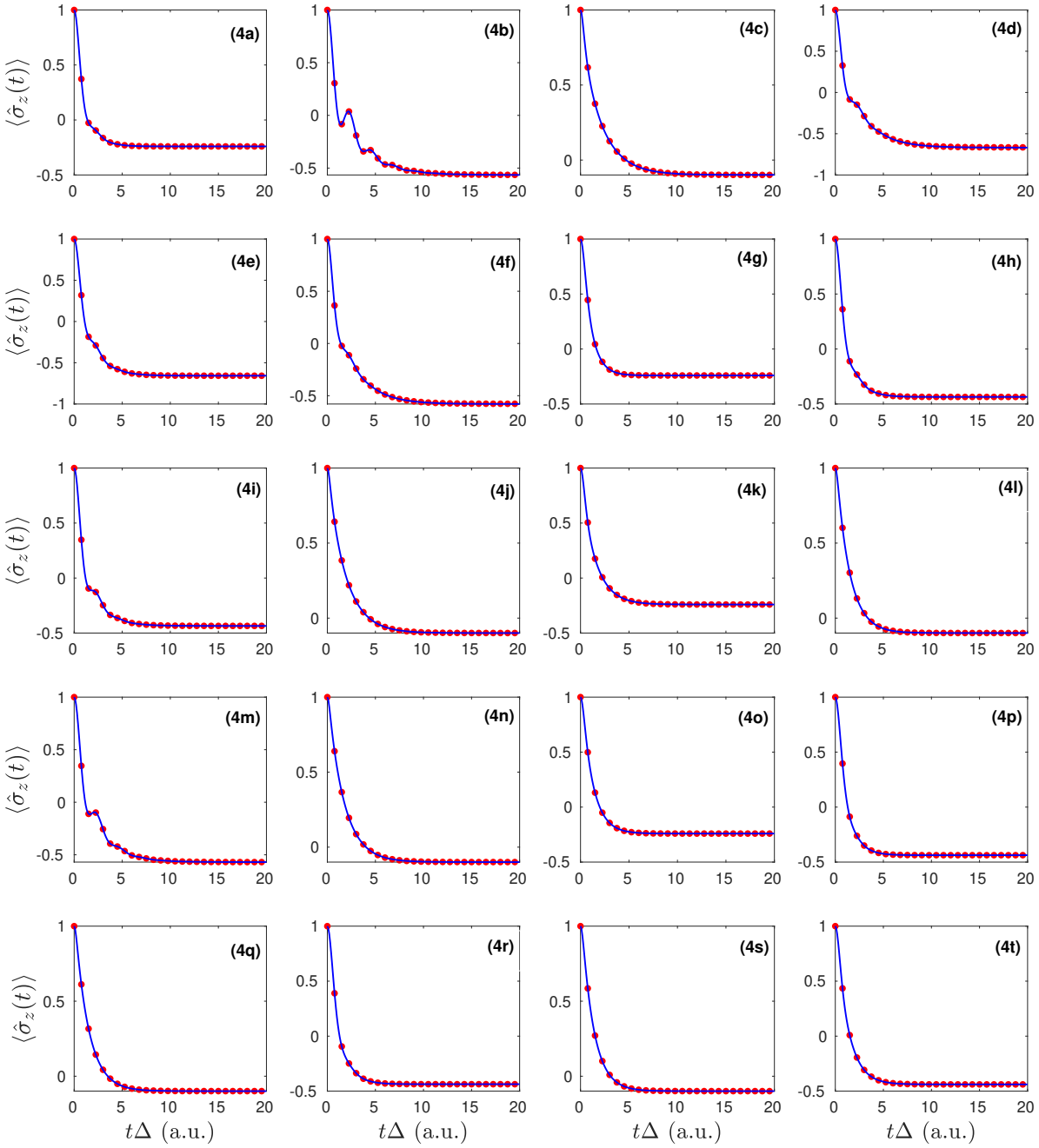

Figure S4: Expectation value of $\hat{\sigma}_z$ for asymmetric SB model as a function of time. Results predicted by KRR model (blue line) are compared to the HEOM results (red dots). The adopted parameters are given in Table S1.

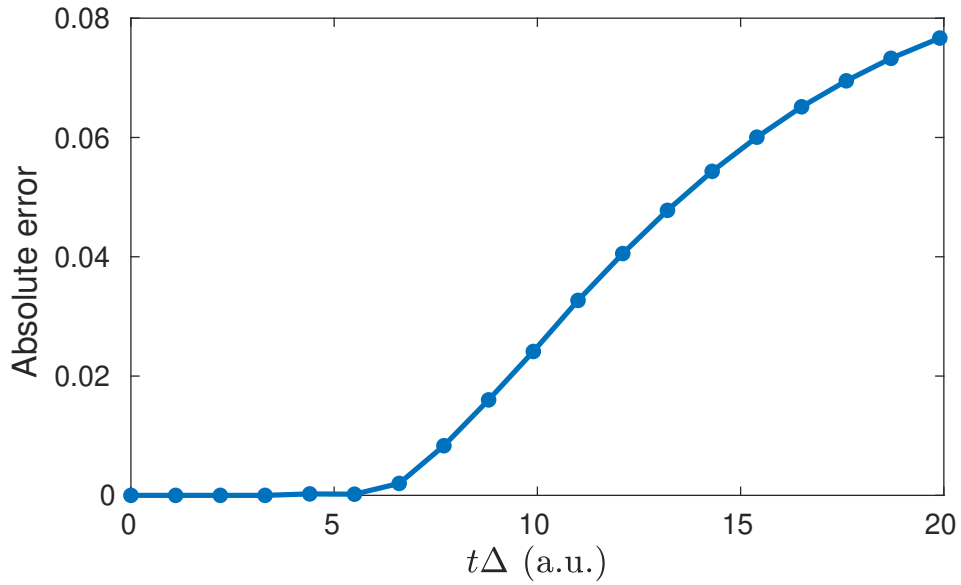

Figure S5: Absolute error $|\langle\hat{\sigma}_z(t)\rangle^{\mathrm{HEOM}} - \langle\hat{\sigma}_z(t)\rangle^{\mathrm{KRR}}|$ for Fig. S3-(3f) as a function of time.